nature geoscience

Article

https://doi.org/10.1038/s41561-025-01812-2

Equatorial upwelling of phosphorus drives Atlantic N_2 fixation and *Sargassum* blooms

Received: 10 January 2025

Accepted: 4 September 2025

Published online: 5 November 2025

Check for updates

Jonathan Jung[1] ✉, Nicolas N. Duprey[1], Alan D. Foreman[1], Juan Pablo D'Olivo[2], Carolin Pellio[1], Yeongjun Ryu[3], Erin L. Murphy[4,5], Baseerat Romshoo[6], Diego K. Kersting[7], Gabriel O. Cardoso[8], Tanja Wald[1], François Fripiat[1,9], Carlos Jimenez[10], Eberhard Gischler[11], Paolo Montagna[12], Carlos Alonso-Hernández[13], Miguel Gomez-Batista[14], Christina Treinen-Crespo[15], José Carriquiry[15,25], Maria Rosabelle Ong[16,17], Nathalie F. Goodkin[17], Reia Guppy[18], Hedy Aardema[1], Hans Slagter[1], Lena Heins[1], Isabella Hrabe de Angelis[6], Aaron L. Bieler[1,19], Maayan Yehudai[1], Trevor P. Noël[20], Kendon James[20], Denis Scholz[21], Chuanmin Hu[22], Brian B. Barnes[22], Andrea Pozzer[23,24], Christopher Pöhlker[6], Jos Lelieveld[23,24], Ulrich Pöschl[6], Hubert Vonhof[1], Gerald H. Haug[1,19], Ralf Schiebel[1], Daniel M. Sigman[3] & Alfredo Martínez-García[1] ✉

The Great Atlantic *Sargassum* Belt first appeared in 2011 and quickly became the largest interconnected floating biome on Earth. In recent years, *Sargassum* stranding events have caused substantial ecological and socio-economic impacts in coastal communities. *Sargassum* requires both phosphorus (P) and nitrogen (N) for growth, yet the primary sources of these nutrients fuelling the extensive *Sargassum* blooms remain unclear. Here we use coral-bound N isotopes to reconstruct N_2 fixation, the ultimate source of the ocean's bioavailable N, across the Caribbean over the past 120 years. Our data indicate that changes in N_2 fixation were primarily controlled by multidecadal and interannual changes in equatorial Atlantic upwelling of 'excess P', that is, P in stoichiometric excess relative to fixed N. We show that the supply of excess P from equatorial upwelling and N from the N_2 fixation response can account for the majority of *Sargassum* variability since 2011. *Sargassum* dynamics are best explained by their symbiosis with N_2-fixing epiphytes, which render the macroalgae highly competitive during strong equatorial upwelling of excess P. Thus, the future of *Sargassum* in the tropical Atlantic will depend on how global warming affects equatorial Atlantic upwelling and the climatic modes that control it.

The Great Atlantic *Sargassum* Belt (GASB)[1] acts as a floating ecosystem for marine life, providing essential food and shelter for important species, such as tuna, marlin, turtles and birds[2,3]. However, at highest abundances, its stranding events burden coastal ecosystems and impair the well-being of coastal communities. During major GASB years, tons of *Sargassum* wash ashore, affect community health and tourism, and require costly management and removal efforts. Decomposing *Sargassum* emits hydrogen sulfide gas, thereby posing widespread health risks that are exacerbated by plastic debris caught in the algae as it travels to the Caribbean[4,5]. Thus, the GASB has strong and complex effects on wildlife and coastal populations.

Historical reports place large quantities of *Sargassum* in the Gulf of Mexico and the Sargasso Sea. In 2010, exceptionally strong westerly winds in the North Atlantic are hypothesized to have caused the export

A full list of affiliations appears at the end of the paper. ✉e-mail: jonathan.jung@mpic.de; a.martinez-garcia@mpic.de

https://doi.org/10.1038/s41561-025-01812-2

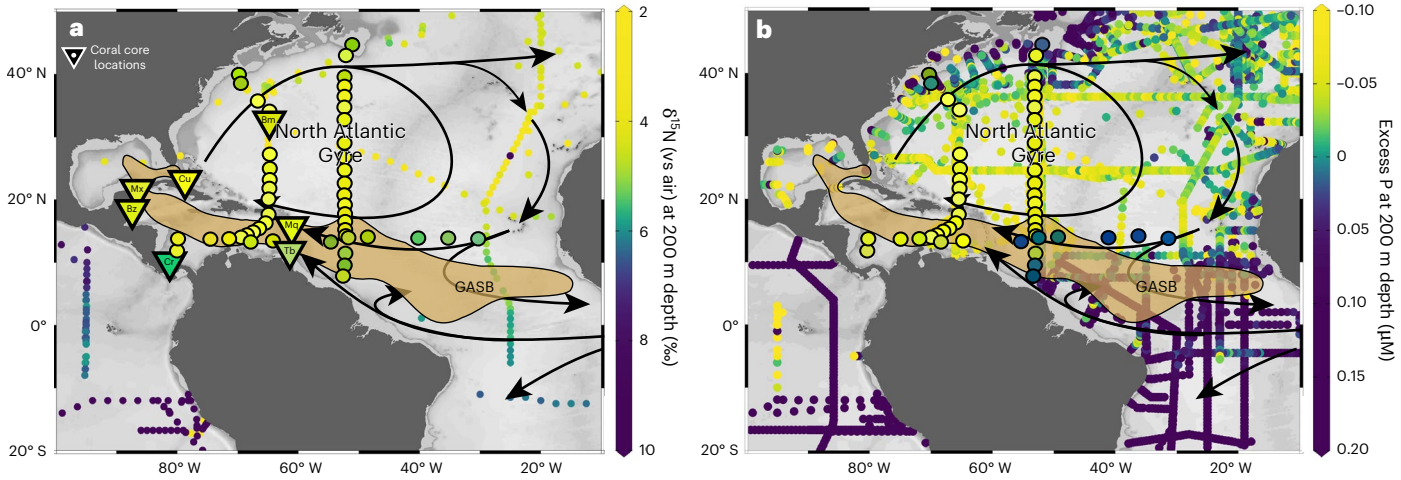

Fig. 1 | Coral core and water sample locations in the wider Caribbean region. **a**,The coral core locations are indicated by large triangles with black outlines, and water samples are denoted by large circles with black outlines. The small circles correspond to previous measurements taken from ref. 40. The colour scale for all symbols shows the nitrate $\delta^{15}N$ (expressed in ‰ with respect to air) at 200 m depth. Coral core sample locations are Hog Reef, Bermuda (Bm: 32.4469° N, 64.8252° W), Cayo Santa María, Cuba (Cu: 22.6677° N, 79.0997° W), Puerto Morelos National Marine Park, Mexico (Mx: 20.8900° N, 86.8100° W), Turneffe Atoll, Belize (Bz: 17.4027° N, 87.8905° W), Caye d'Olbian, Martinique (Mq: 14.4669° N, 61.0164° W), Little Tobago Island, Trinidad and Tobago (Tb: 11.2986° N, 60.5083° W) and Cahuita, Costa Rica (Cr: 9.7514° N, 82.8192° W). **b**, Water-column excess P (in μM; expressed as P*, which equals $PO_4^{3-} - NO_3^-/16$) at 200 m depth, based on the GLODAPv2.2022 dataset[76]. Newly measured nitrate $\delta^{15}N$ and P* values from an east–west transect at 13° N were obtained on the sailing yacht *Eugen Seibold* during the expedition of December–March 2022/2023, and data from north–south transects were obtained on the GO-SHIP A20 (16 March to 16 April 2021) and A22 (20 April to 16 May 2021) sections. New data are indicated as large circles with black outlines, and these are plotted on the same scale as the global dataset. Both panels include the prevailing surface currents (black arrows) and the extent of the GASB (brown shaded area). Basemaps created with Ocean Data View v.5.6.3 (https://odv.awi.de).

of *Sargassum* from the Sargasso Sea to the tropical Atlantic, where it has since been seasonally aggregated by the intertropical convergence zone (ITCZ)[6]. Since then, a noticeable increase in *Sargassum* blooms has been observed in the equatorial Atlantic, leading to more frequent stranding events across Caribbean islands[7]. The magnitude of *Sargassum* blooms is modulated interannually by various physical oceanic processes, with record-high biomasses observed in 2015, 2018, 2021 and 2022[1,5,7,8]. There is a general consensus that shifts in nutrient availability govern the recent surge in *Sargassum* blooms[1,9,10]. However, the origin and dynamics of the nutrient sources that drive the episodic nature of the GASB and the relative importance of the different nutrients are yet to be resolved[1,9–12].

The tropical North Atlantic is widely recognized as conducive to dinitrogen (N_2) fixation[13,14], both with regard to its warm, sunlit, well-stratified surface layer[15,16] and the supply of nutrients. Equatorial Atlantic upwelling and the northwestward flow of the South Equatorial Current carry excess P into the tropical North Atlantic and the Caribbean region (Fig. 1). Whereas aeolian dust fluxes are limited in the southern equatorial Atlantic, high fluxes of dust from the Sahara and Sahel region supply abundant iron to the surface and subsurface waters of the (sub)tropical North Atlantic, even reaching the far western Atlantic Ocean and Caribbean Sea[17,18]. In the context of high iron availability, the supply of excess P appears to drive much of the N_2 fixation in the Caribbean region today[19–23], and geochemical evidence suggests that excess P supply has similarly controlled N_2 fixation in this region over the past 160,000 years[24].

The growth of *Sargassum* in the Caribbean region requires the supply of the macronutrients N and P[1,9,10,25]. To maintain high growth rates, *Sargassum* utilizes P, for example, to produce ribosomal RNA[26,27]. In general, photosynthetic autotrophs in the low-latitude ocean rely largely on one of three N sources: (1) nitrate transported from the subsurface, (2) N that is recycled (largely as ammonium) from heterotrophic metabolism at the surface and (3) autotrophic 'N_2 fixation', the conversion of N_2 to ammonium. The ^{15}N-to-^{14}N isotope ratios of *Sargassum* in the Sargasso Sea are remarkably similar to those of prokaryotic phytoplankton that rely predominantly on recycled N[28]. However, the ^{15}N-to-^{14}N ratio of newly fixed N falls within the same range (Extended Data Fig. 1), and *Sargassum* is known to maintain an association with epiphytic N_2-fixing bacteria, which transfer newly fixed N directly to *Sargassum*, possibly in exchange for P[12,29,30]. Thus, *Sargassum* probably acquires N through both recycled N and epiphytic N_2 fixation, with the latter representing a potential competitive advantage over non-fixing phytoplankton in P-bearing, N-poor environments (that is, in the presence of excess P, that is, positive P*, where $P^* = PO_4^{3-} - NO_3^-/16$)[19,31]. Such a special strategy is particularly pertinent to seaweeds such as *Sargassum*, which have a higher N:P ratio than phytoplankton[9,10]. Thus, the mutualistic relationship of *Sargassum* with epiphytic N_2-fixing cyanobacteria may allow *Sargassum* to occupy the same niche as common phytoplanktonic N_2 fixers found across the Atlantic Ocean. However, little information is known about ongoing variations in N_2 fixation in the region, its relationship to other nutrients or its relevance to recent GASB blooms.

In this Article we use the N isotopic composition of coral-bound organic matter to reconstruct recent changes in Caribbean N_2 fixation. We measured the ^{15}N-to-^{14}N ratio of coral-bound organic matter (expressed as CB-$\delta^{15}N = [(^{15}N/^{14}N)_{sample}/(^{15}N/^{14}N)_{air} - 1] \times 1{,}000‰$) from continuous coral cores spanning the period 1900–2021, with subannual to annual resolution from six locations across the Caribbean Sea (Cuba, Belize, Martinique, Mexico, Tobago and Costa Rica). We interpret these data in the context of tropical Atlantic pycnocline P* values, which both influence and are altered by N_2 fixation (Fig. 1). We find a close coupling between reconstructed N_2 fixation, the supply of excess P to the tropical North Atlantic/Caribbean, and *Sargassum* blooms over recent decades.

Coral-bound nitrogen isotopes as a tracer of N_2 fixation

The production and remineralization of plankton organic matter generally results in an oceanic dissolved N:P ratio of ~16:1, also known as the Redfield ratio[32]. Deviations from the stoichiometric Redfield ratio can be driven by net inputs and losses of N through N_2 fixation and denitrification, respectively[19,33]. N_2 fixation increases the bioavailability of N relative to P (N:P > 16)[15,34], whereas sedimentary and water-column denitrification reduce the bioavailability of N relative to P (N:P < 16). As such, denitrification generates excess P, which in turn favours diazotrophic

https://doi.org/10.1038/s41561-025-01812-2

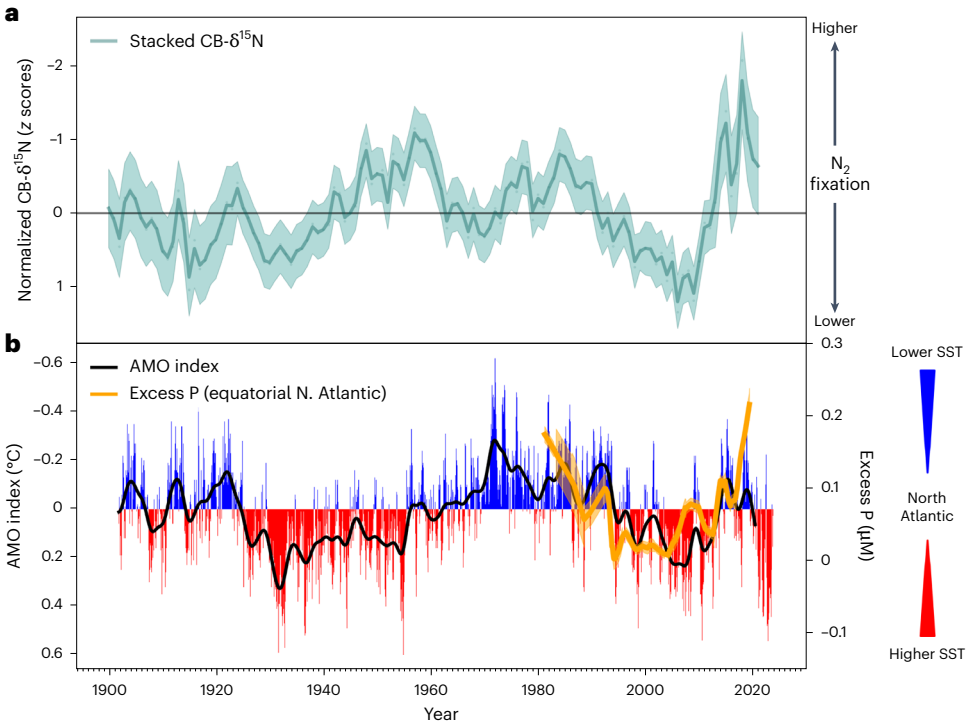

Fig. 2 | CB-δ^{15}N master record and comparison to the AMO. a, The normalized master CB-δ^{15}N record (*z* scores) with the propagated error (±1s.d., shaded region) is based on four coral cores (Belize, Cuba, Martinique and Mexico from 1900 to 2021) from the wider Caribbean region and is closely related to Caribbean nitrate δ^{15}N. Higher normalized CB-δ^{15}N values correspond to lower rates of N_2 fixation, whereas lower normalized CB-δ^{15}N values are indicative of higher N_2 fixation rates. **b**, Compared with **a** is the AMO index derived from Trenberth and Shea[52] (black line) and the locally estimated scatterplot smoothing (LOESS) of depth-integrated P* values of the equatorial North Atlantic (−10 to 30° N, 20 to 60° W) from the GLODAPv2.2022 dataset for the period of 1981–2020 (orange line). The mean LOESS-smoothed P* values show congruent variability with the AMO. Positive AMO phases (red bars) represent a warmer North Atlantic compared with the South Atlantic, whereas negative AMO phases (blue bars) represent a colder North Atlantic compared with the South Atlantic. The positive AMO states correspond to a northward displacement of the ITCZ; negative AMO states indicate a southward displacement of the ITCZ.

growth when sufficient iron is available, ultimately replacing lost N[19]. This response of N_2 fixation to N losses due to denitrification is important in maintaining the marine global N inventory and couples it to P on adequately long timescales[15,24,35,36], whereas spatial aspects of this coupling are influenced by iron availability[20–22].

The stable isotopes of N record changes in the global marine N cycle[37,38]. N_2 fixation introduces fixed N into the ocean with a δ^{15}N value of around −1‰ (ref. 39), which is lower than that of mean global pycnocline nitrate (~6.2‰ (ref. 40)), thereby enabling the identification[41], rate estimation[20] and reconstruction[38] of N_2 fixation. The isotopic impact of denitrification depends on whether it occurs in the water column or in seafloor sediments[19,42]. Water-column denitrification occurs in the oxygen-deficient zones of the ocean and selectively removes ^{14}N-nitrate, thereby increasing the δ^{15}N of the ocean nitrate pool relative to the δ^{15}N of newly fixed N[39,40]. By contrast, sedimentary denitrification consumes most of the nitrate diffusing into sediment pore waters, minimizing the escape of ^{15}N-enriched residual nitrate into the overlying water column[43]. As a result, sedimentary denitrification lowers the N:P ratio of ocean waters with little isotopic effect[44].

The CB-δ^{15}N of symbiont-bearing corals is sensitive to the δ^{15}N of the fixed N supplied to the typically nutrient-poor, oligotrophic reef environments in which they live[45,46]. In areas with high N_2-fixation rates, such as the western tropical North Atlantic, newly fixed N lowers the δ^{15}N of the fixed N pool[41,42], which can be tracked via CB-δ^{15}N (Fig. 1a)[47]. CB-δ^{15}N is largely protected from post-depositional alteration, making it a reliable tool for assessing processes in the marine N cycle[48], even in fossil Palaeozoic corals[49,50].

The CB-δ^{15}N values of our Caribbean records range from 1.87‰ to 6.68‰ (Extended Data Fig. 2). The lowest average values obtained are from Cuba (2.85 ± 0.41‰), and the highest average values are found in Costa Rica (5.09 ± 0.55‰). The average CB-δ^{15}N from Cuba, Martinique (3.01 ± 0.25‰), Belize (3.33 ± 0.36‰) and Mexico (3.67 ± 0.23‰) agree with the measured mean Caribbean nitrate δ^{15}N (3.28 ± 0.76‰). The average CB-δ^{15}N values at Tobago (4.60 ± 0.31‰) and Costa Rica are above the mean Caribbean nitrate δ^{15}N. The relatively high CB-δ^{15}N at Tobago is consistent with its southeastward location, in the path of the Brazil Current that carries higher δ^{15}N nitrate and organic N northwestwards from the equatorial Atlantic into the Caribbean (Fig. 1a), with much of the tropical North Atlantic N_2 fixation occurring downstream of this[20]. The high CB-δ^{15}N from the Costa Rican margin is probably due to local coastal processes, including possible anthropogenic influences (Supplementary Discussion). The CB-δ^{15}N time series from Belize, Cuba, Martinique and Mexico may also be influenced by local processes during some periods, but they show remarkable similarities in their multidecadal variability when normalized (Extended Data Fig. 3). We analysed the underlying shared natural variability of those four records by normalizing and smoothing them with a Gaussian filter (Methods). The normalized records are then combined into a master chronology to evaluate the variability of N_2 fixation in the Caribbean region from 1900 to 2021 (Fig. 2).

Multidecadal modulation of N_2 fixation

The normalized master CB-δ^{15}N record shows multidecadal variability, with dominant 16-, 32- and 64-year cycles that are characteristic of the Atlantic Multidecadal Oscillation (AMO) (Fig. 2 and Extended Data Fig. 4). The AMO index represents multidecadal sea surface temperature (SST) variability in the North Atlantic[51,52], whereas the Atlantic Meridional Mode (AMM) index traces the higher-frequency mode of SST variability[53,54]. Atlantic SST variability is linked to changes

https://doi.org/10.1038/s41561-025-01812-2

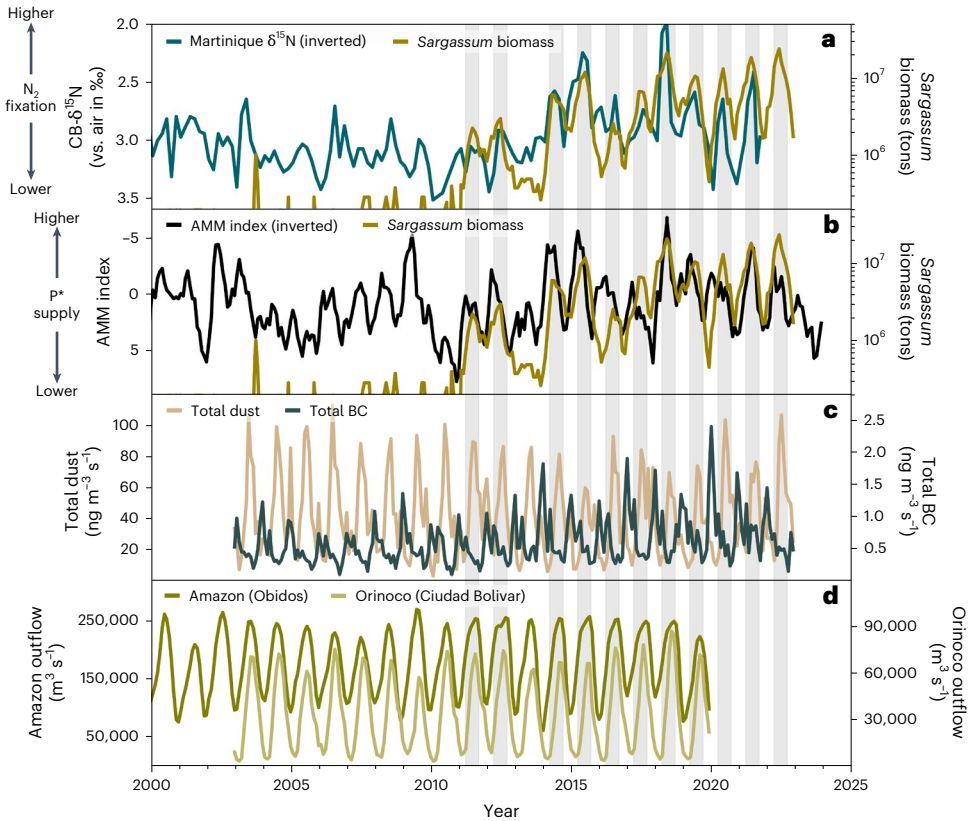

Fig. 3 | Seasonal CB-δ^{15}N values from Martinique compared with *Sargassum* biomass and environmental parameters. a, CB-δ^{15}N values (versus air) of the coral core collected in Martinique from 2000 to 2021 compared with the biomass of *Sargassum* spp (plotted in a logarithmic scale). **b**, Inverted AMM index based on Chiang and Vimont[53] for the 2000–2024 period compared with the biomass of *Sargassum* spp (plotted in a logarithmic scale). More negative AMM states correspond to a southward displacement of the ITCZ, stronger easterlies, enhanced equatorial upwelling and a weakened NECC, which result in greater supply of excess P to the Caribbean. **c**, Area-weighted Atlantic (10 to 20° N, 20 to 60° W) total dust deposition and total black carbon (BC) deposition calculated using the ECHAM5/MESSy Atmospheric Chemistry (EMAC) model. **d**, Monthly discharge for the Amazon River measured at the Óbidos gauge station (1.92° S, 55.67° W) and for the Orinoco River measured at the Ciudad Bolivar gauge station (8.15° N, 63.54° W) obtained from SO-HYBAM material-transport datasets. In all panels, the vertical grey bars mark the *Sargassum* spp. peak seasons (April to September) since 2011.

in atmospheric and oceanic circulation, the position of the ITCZ and the corresponding location and strength of surface winds over the Atlantic[55]. Multidecadal variability has been reconstructed with SST proxies in coral cores[56,57], speleothems[58] and sediment cores[59] throughout the Caribbean, demonstrating a connection between basin-scale variability and local climate conditions, but its potential influence on N_2 fixation has not been investigated.

Anomalous cold North Atlantic and warm South Atlantic SSTs, which correspond, respectively, to a negative AMO/AMM index and a strengthened Hadley cell in the Southern Hemisphere, result in a southward displacement of the ITCZ[55,60,61]. Under these conditions, trade winds (easterlies) are maximal and enhance equatorial upwelling, the strength of the South Equatorial Current and the Caribbean Current (Extended Data Fig. 5)[17,18,24]. By contrast, positive AMO/AMM phases are characterized by a northward displacement of the ITCZ[62], weaker easterlies, reduced equatorial upwelling and an enhanced North Equatorial Counter Current (NECC)[63].

Upwelled waters in the equatorial North Atlantic tend to be depleted in nitrate compared with phosphate due to their origins in the Southern Ocean and Indo-Pacific[19], and thus contain higher excess P than Caribbean water masses[19,33] (Fig. 1 and Extended Data Fig. 6). Measurements of excess P over the past decades are spatially scarce and temporally discontinuous. Nevertheless, a compilation of the available data from multiple oceanographic cruises shows that the concentration of excess P in the equatorial North Atlantic is closely coupled with multidecadal variability, with negative AMO states corresponding to enhanced supply of excess P (Fig. 2b).

Variations in our master CB-δ^{15}N record show a significant positive correlation with the AMO index for the period between 1900 and 1972 (adjusted $r^2 = 0.33$, $P < 0.01$) and a higher correlation from 1972 to 2021 (adjusted $r^2 = 0.60$, $P < 0.01$), when the AMO and AMM are in phase (Fig. 2 and Extended Data Fig. 7), consistent with an anthropogenically forced AMO-like signal in the modern era[64]. Negative CB-δ^{15}N anomalies, which are indicative of enhanced N_2 fixation, align with negative AMO phases when a southward displacement of the ITCZ leads to enhanced equatorial upwelling. Strengthened easterlies and the Caribbean Current, in turn, would allow upwelled waters to penetrate into the Caribbean Basin more effectively. The correlation between our CB-δ^{15}N and the AMO indicates that the supply of excess P has controlled N_2 fixation in the Caribbean over the past 120 years.

A remarkable aspect of our findings is their consistency with previous findings regarding Caribbean N_2-fixation changes on the vastly different timescales of the Earth's orbital cycles[24]. As with AMO, precession drives cycles in equatorial Atlantic upwelling[65], and the phases of more vigorous upwelling are associated with maxima in N_2 fixation[24]. From the perspective of the ~22,000-year precession cycle, Caribbean N_2 fixation is currently near maximal rates, with AMO further modulating N_2 fixation.

Linking excess phosphorus supply, N_2 fixation and *Sargassum* blooms

The biomass of floating *Sargassum* has been continuously mapped and quantified since 2000 (Fig. 3a,b)[66]. Changes in macro- and micro-nutrient availability have been suggested as driving recent increases in *Sargassum*

biomass[1,9,10]. However, there is disagreement as to the sources and mechanisms behind the post-2011 GASB. Proposals have included nutrient inputs from atmospheric deposition, rivers and oceanic changes[1,9].

Our high-resolution CB-$\delta^{15}N$ record of N_2 fixation from Martinique shows a positive correlation with the reconstructed log-transformed *Sargassum* biomass from 2011 to 2021 (adjusted $r^2 = 0.51$, $P < 0.01$). In addition, the first two extreme *Sargassum* blooms in 2015 and 2018 coincide with the highest rates of N_2 fixation of the past 120 years (Figs. 2 and 3a). The interannual coupling between N_2 fixation and *Sargassum* blooms appears to be modulated by the AMM (Fig. 3a,b). The AMM is correlated with changes in log-transformed *Sargassum* biomass (adjusted $r^2 = 0.30$, $P < 0.01$) and N_2 fixation (adjusted $r^2 = 0.32$, $P < 0.01$) since the first appearance of the GASB in 2011. The negative phase of the AMM is associated with negative SST anomalies near 10° N, corresponding to a southward displacement of the ITCZ that leads to unusually strong trade winds near 5° N[53,67]. The AMM typically reaches a minimum in the boreal spring when the GASB starts to bloom. During negative AMM states, the seasonal development of the NECC along 5–10° N in the second half of the year connects *Sargassum* to the shallower mixed layer around the Guinea Dome during late autumn[54,67,68], potentially also explaining the emergence of long *Sargassum* bands during the second half of the year (Extended Data Fig. 8).

The evidence that an increased supply of excess P (negative AMM) both enhances N_2 fixation and encourages *Sargassum* blooms indicates a mechanism linking the two. The average N retained in *Sargassum* biomass (0.91 µmol N m^{-2}) is much smaller than the surface particulate N pool suspended in the mixed layer (~30 mmol N m^{-2}), such that the supply of recycled N to the surface mixed layer is far in excess of that required for *Sargassum* growth. This implies that *Sargassum* is not a major competitor for recycled N in surface waters. Accordingly, the increased supply of recycled N that accompanies periods of rapid N_2 fixation cannot explain *Sargassum* blooms. Rather, the explosive growth of *Sargassum* is probably driven by the N_2 fixation of its epiphytes, which can channel their newly fixed N directly to their host. That is, *Sargassum* appears to occupy the same niche as other diazotrophs in the tropical North Atlantic[12,29,30], acting de facto as an N_2 fixer itself. This perspective also explains why *Sargassum* accumulations are much stronger in the equatorial North Atlantic compared with previous blooms in the Sargasso Sea. N_2 fixation in the modern Sargasso Sea is currently occurring at a very limited rate[20,41], potentially due to a lower excess P supply[19]. Thus, *Sargassum*, with its limited capacity to compete with phytoplankton for recycled N, was unable to reach biomass accumulations in the Sargasso Sea that are comparable to the GASB.

High rates of N_2 fixation in the Caribbean region are also evident during negative phases of the AMO before 2011 (Figs. 2 and 3b), which indicates that *Sargassum* was only governed by these dynamics once it reached the equatorial North Atlantic. Before this import, there is no evidence of comparable *Sargassum* blooms in the area. Thus, we suggest that the arrival of *Sargassum* in the equatorial North Atlantic triggered the GASB, by making it more proximal to equatorial upwelling, giving *Sargassum* greater access to the excess P supply.

Other environmental parameters and *Sargassum*

Other proposed drivers of *Sargassum* since 2011 include Amazon–Orinoco discharge, black carbon deposition, Saharan dust, atmospheric N and warmer SSTs[1,9,11]. However, their variability is largely seasonal, with negligible interannual fluctuations, and thus cannot explain the observed interannual biomass trends and amplitudes.

There is no interannual relationship between *Sargassum* biomass and Amazon (adjusted $r^2 = 0.06$, $P > 0.05$) or Orinoco (adjusted $r^2 = 0.01$, $P > 0.10$) water/nutrient discharge[9] (Fig. 3d), perhaps because these discharges are restricted to coastal regions whereas most of the *Sargassum* biomass is found in open waters. During the *Sargassum* blooms in 2011 and 2012, satellite observations indicate that *Sargassum* accumulated near the river outflows and was then exported to the equatorial region and the Caribbean[7]. Thus, excess P from the Amazonas may have stimulated N_2 fixation and *Sargassum* in 2011 and 2012[69], analogous to the blooms of the diatom *Richelia intracellularis*—with N_2-fixing endosymbionts—found in the North Brazil margin[70]. Atmospheric N deposition is highest near continents[71], but it is four orders of magnitude lower than naturally occurring open-ocean N_2 fixation[20,72] and appears not to be a viable driver of *Sargassum* blooms (Extended Data Fig. 9). Previous studies have attributed the variability in N:P ratios in *Sargassum* biomass over the past decades to anthropogenic N or P inputs[9,10,73]. However, *Sargassum* N:P ratios align closely with the N:P ratio of upwelled water, with a positive offset (Extended Data Fig. 10). Furthermore, the higher N:P ratios in *Sargassum*[9,10] suggest that its relationship with N_2-fixing symbionts is central to fulfilling its N requirements, especially in environments of high excess P.

We find only a weak correlation of *Sargassum* biomass with the modelled area-weighted deposition of wet dust (adjusted $r^2 = 0.04$, $P > 0.05$), dry dust (adjusted $r^2 = 0.04$, $P < 0.01$), wet black carbon (adjusted $r^2 = 0.08$, $P > 0.05$) or dry black carbon (adjusted $r^2 = 0.14$, $P < 0.01$). Although dry dust and dry black carbon deposition are correlated to *Sargassum* biomass, the relationship is negative, inconsistent with an important role for nutrients from these sources[74]. Regarding the potential role of SST and sea surface salinity (SSS)[11], in situ experiments show optimal *Sargassum* growth at high temperatures (from ~23 to 28 °C) and salinities above 34 PSU (practical salinity units)[1,75]. In the equatorial North Atlantic, SST and SSS are in this range and show no correlation with *Sargassum* biomass (SST: adjusted $r^2 = 0.06$, $P < 0.01$; SSS: adjusted $r^2 = 0.07$, $P < 0.05$) (Supplementary Fig. 1).

Using an Akaike information criterion (AIC), we find that CB-$\delta^{15}N$ and AMM can explain 56% of *Sargassum* biomass from 2011 to 2021 (Supplementary Table 1). Adding any alternative nutrient sources did not improve the AIC, underscoring excess-P-driven N_2 fixation as the dominant driver of *Sargassum* blooms.

Implications for future *Sargassum* blooms

In the tropical Atlantic, wind-driven equatorial upwelling and northward transport of excess P, in the context of a high aeolian iron supply, enhances N_2 fixation. The resulting increase in the supply of both P and N has allowed *Sargassum* to expand since 2011, when the macroalgae were imported from the Sargasso Sea. Since then, negative AMM states have aligned with periods of high *Sargassum* biomass. Thus, the AMM can be used to better predict the annual extent of *Sargassum* blooms in the future, supporting efforts to mitigate the impacts of *Sargassum* blooms on Caribbean reef ecosystems and coastal communities.

Online content

Any methods, additional references, Nature Portfolio reporting summaries, source data, extended data, supplementary information, acknowledgements, peer review information; details of author contributions and competing interests; and statements of data and code availability are available at https://doi.org/10.1038/s41561-025-01812-2.

References

1. Wang, M. et al. The great Atlantic *Sargassum* belt. *Science* **365**, 83–87 (2019).
2. Rooker, J. R., Turner, J. P. & Holt, S. A. Trophic ecology of *Sargassum*-associated fishes in the Gulf of Mexico determined from stable isotopes and fatty acids. *Mar. Ecol. Prog. Ser.* **313**, 249–259 (2006).
3. Witherington, B., Hirama, S. & Hardy, R. Young sea turtles of the pelagic *Sargassum*-dominated drift community: habitat use, population density, and threats. *Mar. Ecol. Prog. Ser.* **463**, 1–22 (2012).
4. Mincer, T. J. et al. Sargasso Sea *Vibrio* bacteria: underexplored potential pathovars in a perturbed habitat. *Water Res* **242**, 120033 (2023).
5. Resiere, D. et al. *Sargassum* seaweed on Caribbean islands: an international public health concern. *Lancet* **392**, 2691 (2018).

6. Johns, E. M. et al. The establishment of a pelagic *Sargassum* population in the tropical Atlantic: biological consequences of a basin-scale long distance dispersal event. *Prog. Oceanogr.* **182**, 102269 (2020).
7. Gower, J., Young, E. & King, S. Satellite images suggest a new *Sargassum* source region in 2011. *Remote Sens. Lett.* **4**, 764–773 (2013).
8. Putman, N. F. & Hu, C. Sinking *Sargassum*. *Geophys. Res. Lett.* **49**, e2022GL100189 (2022).
9. Lapointe, B. E. et al. Nutrient content and stoichiometry of pelagic *Sargassum* reflects increasing nitrogen availability in the Atlantic Basin. *Nat. Commun.* **12**, 3060 (2021).
10. McGillicuddy, D. J. Jr et al. Nutrient and arsenic biogeochemistry of *Sargassum* in the western Atlantic. *Nat. Commun.* **14**, 6205 (2023).
11. Djakouré, S., Araujo, M., Hounsou-Gbo, A., Noriega, C. & Bourlès, B. On the potential causes of the recent Pelagic *Sargassum* blooms events in the tropical North Atlantic Ocean. Preprint at *Biogeosciences* https://doi.org/10.5194/bg-2017-346 (2017).
12. Johnson, C., Dubbs, L. L. & Piehler, M. Reframing the contribution of pelagic *Sargassum* epiphytic N_2 fixation. *PLoS ONE* **18**, e0289485 (2023).
13. Carpenter, E. J. et al. Extensive bloom of a N_2-fixing diatom/cyanobacterial association in the tropical Atlantic Ocean. *Mar. Ecol. Prog. Ser.* **185**, 273–283 (1999).
14. Luo, Y.-W. et al. Database of diazotrophs in global ocean: abundance, biomass and nitrogen fixation rates. *Earth Syst. Sci. Data* **4**, 47–73 (2012).
15. Gruber, N. Consistent patterns of nitrogen fixation identified in the ocean. *Nature* **566**, 191–193 (2019).
16. Zehr, J. P. & Capone, D. G. Changing perspectives in marine nitrogen fixation. *Science* **368**, eaay9514 (2020).
17. van der Does, M., Brummer, G.-J. A., Korte, L. F. & Stuut, J.-B. W. Seasonality in Saharan dust across the Atlantic Ocean: from atmospheric transport to seafloor deposition. *J. Geophys. Res. Atmos.* **126**, e2021JD034614 (2021).
18. van der Does, M. et al. Tropical rains controlling deposition of Saharan dust across the North Atlantic Ocean. *Geophys. Res. Lett.* **47**, e2019GL086867 (2020).
19. Deutsch, C., Sarmiento, J. L., Sigman, D. M., Gruber, N. & Dunne, J. P. Spatial coupling of nitrogen inputs and losses in the ocean. *Nature* **445**, 163–167 (2007).
20. Marconi, D. et al. Tropical dominance of N_2 fixation in the North Atlantic Ocean. *Global Biogeochem. Cycles* **31**, 1608–1623 (2017).
21. Moore, C. M. et al. Large-scale distribution of Atlantic nitrogen fixation controlled by iron availability. *Nat. Geosci.* **2**, 867–871 (2009).
22. Schlosser, C. et al. Seasonal ITCZ migration dynamically controls the location of the (sub)tropical Atlantic biogeochemical divide. *Proc. Natl Acad. Sci. USA* **111**, 1438–1442 (2014).
23. Wu, J., Sunda, W., Boyle, E. A. & Karl, D. M. Phosphate depletion in the western North Atlantic Ocean. *Science* **289**, 759–762 (2000).
24. Straub, M. et al. Changes in North Atlantic nitrogen fixation controlled by ocean circulation. *Nature* **501**, 200–203 (2013).
25. Lapointe, B. E. Phosphorus-limited photosynthesis and growth of *Sargassum natans* and *Sargassum fluitans* (Phaeophyceae) in the western North Atlantic. *Deep Sea Res. A* **33**, 391–399 (1986).
26. Hillebrand, H. et al. Goldman revisited: faster-growing phytoplankton has lower N:P and lower stoichiometric flexibility. *Limnol. Oceanogr.* **58**, 2076–2088 (2013).
27. Elser, J. J. et al. Growth rate–stoichiometry couplings in diverse biota. *Ecol. Lett.* **6**, 936–943 (2003).
28. Fawcett, S. E. & Ward, B. B. Phytoplankton succession and nitrogen utilization during the development of an upwelling bloom. *Mar. Ecol. Prog. Ser.* **428**, 13–31 (2011).
29. Carpenter, E. J. Nitrogen fixation by a blue-green epiphyte on pelagic. *Sargassum*. *Science* **178**, 1207–1209 (1972).
30. Cox, D. D., Parsons, R. J., Van Mooy, B. A. S. & Valentine, D. L. Methylphosphonate is utilized by commensal microbiota of macroalgae in the oligotrophic Sargasso Sea. *J. Geophys. Res. Oceans* **128**, e2023JC020315 (2023).
31. Fawcett, S. E., Lomas, M. W., Casey, J. R., Ward, B. B. & Sigman, D. M. Assimilation of upwelled nitrate by small eukaryotes in the Sargasso Sea. *Nat. Geosci.* **4**, 717–722 (2011).
32. Redfield, A. C. The biological control of chemical factors in the environment. *Am. Sci.* **46**, 205–221 (1958).
33. Gruber, N. & Sarmiento, J. L. Global patterns of marine nitrogen fixation and denitrification. *Global Biogeochem. Cycles* **11**, 235–266 (1997).
34. Mahaffey, C., Michaels, A. F. & Capone, D. G. The conundrum of marine N_2 fixation. *Am. J. Sci.* **305**, 546–595 (2005).
35. Ren, H. et al. Impact of glacial/interglacial sea level change on the ocean nitrogen cycle. *Proc. Natl Acad. Sci. USA* **114**, E6759–E6766 (2017).
36. Ustick, L. J. et al. Metagenomic analysis reveals global-scale patterns of ocean nutrient limitation. *Science* **372**, 287–291 (2021).
37. Altabet, M. A. & Francois, R. The use of nitrogen isotopic ratio for reconstruction of past Changes in surface ocean nutrient utilization. In *Carbon Cycling in the Glacial Ocean: Constraints on the Ocean's Role in Global Change* (eds Zahn, R. et al.) 281–306 (Springer, 1994); https://doi.org/10.1007/978-3-642-78737-9_12.
38. Ren, H. et al. Foraminiferal isotope evidence of reduced nitrogen fixation in the ice age Atlantic Ocean. *Science* **323**, 244–248 (2009).
39. Fripiat, F. et al. The impact of incomplete nutrient consumption in the Southern Ocean on global mean ocean nitrate $\delta^{15}N$. *Global Biogeochem. Cycles* **37**, e2022GB007442 (2023).
40. Fripiat, F. et al. Nitrogen isotopic constraints on nutrient transport to the upper ocean. *Nat. Geosci.* **14**, 855–861 (2021).
41. Knapp, A. N., Sigman, D. M. & Lipschultz, F. N isotopic composition of dissolved organic nitrogen and nitrate at the Bermuda Atlantic Time-series Study site. *Global Biogeochem. Cycles* https://doi.org/10.1029/2004GB002320 (2005).
42. Knapp, A. N., DiFiore, P. J., Deutsch, C., Sigman, D. M. & Lipschultz, F. Nitrate isotopic composition between Bermuda and Puerto Rico: implications for N_2 fixation in the Atlantic Ocean. *Global Biogeochem. Cycles* https://doi.org/10.1029/2007GB003107 (2008).
43. Lehmann, M. F. et al. The distribution of nitrate $^{15}N/^{14}N$ in marine sediments and the impact of benthic nitrogen loss on the isotopic composition of oceanic nitrate. *Geochim. Cosmochim. Acta* **71**, 5384–5404 (2007).
44. Brandes, J. A. & Devol, A. H. Isotopic fractionation of oxygen and nitrogen in coastal marine sediments. *Geochim. Cosmochim. Acta* **61**, 1793–1801 (1997).
45. Wang, X. T. et al. Influence of open ocean nitrogen supply on the skeletal $\delta^{15}N$ of modern shallow-water scleractinian corals. *Earth Planet. Sci. Lett.* **441**, 125–132 (2016).
46. Wang, X. T. et al. Isotopic composition of skeleton-bound organic nitrogen in reef-building symbiotic corals: a new method and proxy evaluation at Bermuda. *Geochim. Cosmochim. Acta* **148**, 179–190 (2015).
47. Wang, X. T. et al. Natural forcing of the North Atlantic nitrogen cycle in the Anthropocene. *Proc. Natl Acad. Sci. USA* **115**, 10606–10611 (2018).
48. Martínez-García, A. et al. Laboratory assessment of the impact of chemical oxidation, mineral dissolution, and heating on the nitrogen isotopic composition of fossil-bound organic matter. *Geochem. Geophys. Geosyst.* **23**, e2022GC010396 (2022).
49. Frankowiak, K. et al. Photosymbiosis and the expansion of shallow-water corals. *Sci. Adv.* **2**, e1601122 (2016).
50. Jung, J. et al. Coral photosymbiosis on Mid-Devonian reefs. *Nature* **636**, 647–653 (2024).
51. McCarthy, G. D., Haigh, I. D., Hirschi, J. J.-M., Grist, J. P. & Smeed, D. A. Ocean impact on decadal Atlantic climate variability revealed by sea-level observations. *Nature* **521**, 508–510 (2015).

52. Trenberth, K. E. & Shea, D. J. Atlantic hurricanes and natural variability in 2005. *Geophys. Res. Lett.* https://doi.org/10.1029/2006GL026894 (2005).
53. Chiang, J. C. H. & Vimont, D. J. Analogous Pacific and Atlantic meridional modes of tropical Atmosphere–ocean variability. *J. Clim.* **17**, 4143–4158 (2004).
54. Vimont, D. J. & Kossin, J. P. The Atlantic Meridional Mode and hurricane activity. *Geophys. Res. Lett.* https://doi.org/10.1029/2007GL029683 (2007).
55. Wu, C.-R., Lin, Y.-F. & Qiu, B. Impact of the Atlantic Multidecadal Oscillation on the Pacific North Equatorial Current bifurcation. *Sci. Rep.* **9**, 2162 (2019).
56. Hetzinger, S. et al. Caribbean coral tracks Atlantic Multidecadal Oscillation and past hurricane activity. *Geology* **36**, 11–14 (2008).
57. von Reumont, J., Hetzinger, S., Garbe-Schönberg, D., Manfrino, C. & Dullo, C. Tracking interannual- to multidecadal-scale climate variability in the Atlantic Warm Pool using Central Caribbean coral data. *Paleoceanogr. Paleoclimatol.* **33**, 395–411 (2018).
58. Fensterer, C. et al. Cuban stalagmite suggests relationship between Caribbean precipitation and the Atlantic Multidecadal Oscillation during the past 1.3 ka. *Holocene* **22**, 1405–1412 (2012).
59. Schmitt, D. et al. Great Blue Hole (Lighthouse Reef, Belize): a continuous, annually-resolved record of Common Era sea surface temperature, Atlantic Multidecadal Oscillation and cyclone-controlled run-off. *Quat. Sci. Rev.* **247**, 106570 (2020).
60. Wang, C. Atlantic climate variability and its associated atmospheric circulation cells. *J. Clim.* **15**, 1516–1536 (2002).
61. Zhou, C., Lu, J., Hu, Y. & Zelinka, M. D. Responses of the Hadley circulation to regional sea surface temperature changes. *J. Clim.* **33**, 429–441 (2020).
62. Williams, R. H. et al. Glacial to Holocene changes in trans-Atlantic Saharan dust transport and dust–climate feedbacks. *Sci. Adv.* **2**, e1600445 (2016).
63. Martín-Rey, M., Vallès-Casanova, I. & Pelegrí, J. L. Upper-ocean circulation and tropical Atlantic interannual modes. *J. Clim.* **36**, 2625–2643 (2023).
64. Mann, M. E., Steinman, B. A., Brouillette, D. J. & Miller, S. K. Multidecadal climate oscillations during the past millennium driven by volcanic forcing. *Science* **371**, 1014–1019 (2021).
65. Molfino, B. & McIntyre, A. Precessional forcing of nutricline dynamics in the equatorial Atlantic. *Science* **249**, 766–769 (1990).
66. Wang, M. & Hu, C. Mapping and quantifying *Sargassum* distribution and coverage in the Central West Atlantic using MODIS observations. *Remote Sens. Environ.* **183**, 350–367 (2016).
67. Doi, T., Tozuka, T. & Yamagata, T. The Atlantic Meridional Mode and its coupled variability with the Guinea Dome. *J. Clim.* **23**, 455–475 (2010).
68. Doi, T., Tozuka, T. & Yamagata, T. Interannual variability of the Guinea Dome and its possible link with the Atlantic Meridional Mode. *Clim. Dyn.* **33**, 985–998 (2009).
69. Härri, J., Louchard, D. & Gruber, N. Interannual variability of marine nitrogen fixation in the western tropical Atlantic. *Global Biogeochem. Cycles* **38**, e2023GB007997 (2024).
70. Weber, S. C. et al. Amazon River influence on nitrogen fixation and export production in the western tropical North Atlantic. *Limnol. Oceanogr.* **62**, 618–631 (2017).
71. Duce, R. A. et al. Impacts of atmospheric anthropogenic nitrogen on the open ocean. *Science* **320**, 893–897 (2008).
72. Altieri, K. E., Fawcett, S. E., Peters, A. J., Sigman, D. M. & Hastings, M. G. Marine biogenic source of atmospheric organic nitrogen in the subtropical North Atlantic. *Proc. Natl Acad. Sci. USA* **113**, 925–930 (2016).
73. Lapointe, B. E., Webber, D. F. & Brewton, R. A. Productivity, growth, and biogeochemistry of pelagic *Sargassum* in a changing world. Harmful Algae **150**, 102940. (2025).
74. Hickman, J. E. et al. Reductions in NO_2 burden over north equatorial Africa from decline in biomass burning in spite of growing fossil fuel use, 2005 to 2017. *Proc. Natl Acad. Sci. USA* **118**, e2002579118 (2021).
75. Hanisak, M. D. & Samuel, M. A. Growth rates in culture of several species of *Sargassum* from Florida, USA. In *Twelfth International Seaweed Symposium* (eds Ragan, M. A. & Bird, C. J.) 399–404 (Springer, 1987); https://doi.org/10.1007/978-94-009-4057-4_59.
76. Olsen, A. et al. The Global Ocean Data Analysis Project version 2 (GLODAPv2)—an internally consistent data product for the world ocean. *Earth Syst. Sci. Data* **8**, 297–323 (2016).

[1]Climate Geochemistry Department, Max Planck Institute for Chemistry, Mainz, Germany. [2]Unidad Académica de Sistemas Arrecifales, Instituto de Ciencias del Mar y Limnología, Universidad Nacional Autónoma de México, Puerto Morelos, Mexico. [3]Department of Geosciences, Princeton University, Princeton, NJ, USA. [4]Ocean Conservancy, Washington, DC, USA. [5]Center for Biodiversity Outcomes, Arizona State University, Tempe, AZ, USA. [6]Multiphase Chemistry Department, Max Planck Institute for Chemistry, Mainz, Germany. [7]Instituto de Acuicultura de Torre de la Sal (CSIC), Ribera de Cabanes, Spain. [8]Institute of Geological Sciences, Freie Universität Berlin, Berlin, Germany. [9]Department of Geosciences, Environment and Society, Université Libre de Bruxelles, Brussels, Belgium. [10]Enalia Physis Environmental Research Centre, Nicosia, Cyprus. [11]Institut für Geowissenschaften, Goethe-Universität Frankfurt am Main, Frankfurt am Main, Germany. [12]Istituto di Scienze Polari (ISP), Consiglio Nazionale delle Ricerche (CNR), Bologna, Italy. [13]IAEA Marine Environment Laboratories, Monaco, Principality of Monaco. [14]Centro de Estudios Ambientales de Cienfuegos (CEAC), Cienfuegos, Cuba. [15]Instituto de Investigaciones Oceanológicas, Universidad Autónoma de Baja California, Ensenada, Mexico. [16]Lamont-Doherty Earth Observatory, Department of Earth and Environmental Sciences, Columbia University, New York, NY, USA. [17]Department of Earth and Planetary Sciences, American Museum of Natural History, New York, NY, USA. [18]Centre for Maritime and Ocean Studies, Marine Sciences, The University of Trinidad and Tobago, Chaguaramas, Trinidad. [19]Department of Earth and Planetary Sciences (D-EAPS), ETH Zürich, Zurich, Switzerland. [20]Windward Islands Research and Education Foundation (WINDREF), St. George's University, True Blue, Grenada. [21]Institute of Geosciences, University of Mainz, Mainz, Germany. [22]College of Marine Science, University of South Florida, St Petersburg, FL, USA. [23]Atmospheric Chemistry Department, Max Planck Institute for Chemistry, Mainz, Germany. [24]Climate and Atmosphere Research Center, The Cyprus Institute, Nicosia, Cyprus. [25]Deceased: José Carriquiry. ✉e-mail: jonathan.jung@mpic.de; a.martinez-garcia@mpic.de

Methods

Coral samples

Coral drill cores were collected between 1997 and 2021 from living colonies of massive corals at multiple locations across the Caribbean by different research groups. An overview of the metadata is given in Supplementary Table 2, and includes coral species, location, depth at which the coral core was sampled, sampling resolution, age model method and the length of the record. Cores were sliced into longitudinal slabs and rinsed with deionized water and sent to the Martínez-García Laboratory at the Max Planck Institute for Chemistry (MPIC) in Mainz for analysis.

Analysis of coral-bound nitrogen isotopes

The CB-$\delta^{15}N$ measurements were performed in the Martínez-García Laboratory (MPIC). We used the persulfate oxidation–denitrifier method[41,77], applied to corals by Wang et al.[46,78], with modifications described by Moretti et al.[79].

A drilling path was drawn based on ultraviolet scans and subsequent pairs of high- and low-density bands on previously bleached and rinsed coral slabs. Sample material was then carefully extracted perpendicular to the main growth axis using a millimetre drill bit attached to a Dremel hand tool. The milled material was vacuumed and the powder was split into fine (5–63 µm) and coarse (>63 µm) size fractions. Aliquots of fine powder and coarse powder were further used for the analysis of oxygen isotope ($\delta^{18}O$) and $\delta^{15}N$ analyses, respectively.

Coarse powder (6 ± 1 mg) was weighed into a 4 ml VWR borosilicate glass vial, which was filled with sodium hypochlorite (4.25 ml) and left on a shaker at 120 revolutions per min for at least 24 h. The sodium hypochlorite was removed the next day with a pre-combusted glass pipette attached to a vacuum line set at 500 mbar. Samples were then rinsed three times with Milli-Q water (4 ml; 18.2 MΩ cm^{-1} at 25 °C) and left to dry at 60 °C overnight.

Once fully dried, the coarse powder (6 ± 0.2 mg) was weighed inside an in-house clean room to minimize contamination. Thereafter, skeletal-bound organic matter was released by dissolving the final amount of material with 4 N hydrochloric acid (45 µl). Concurrently, a persulfate oxidative reactant solution was prepared inside the clean room using 6.25 N sodium hydroxide (a 4 ml spike) to reach high pH. Persulfate oxidative reactant solution (1 ml) was added to each dissolved sample and at least ten empty cleaned vials (blanks), and the batch of vials was placed in a custom-built sample rack that was tightly sealed with a polytetrafluoroethylene sheet before being autoclaved at 121 °C for 65 min.

A 1 ml volume of concentrated denitrifying bacteria (*Pseudomonas chlororaphis*) was injected into growth medium (800 ml) and left for 4–6 d to grow in the dark at room temperature on a shaking rack. Once the bacteria had grown sufficiently, the medium was transferred to autoclaved polyethylene bottles and centrifuged at ~8,800 × *g* for 10 min. The supernatant was then discarded and the remaining bacteria pellet was resuspended in a buffered (pH 6.3) resuspension medium. From this, 3 ml aliquots were pipetted into separate muffled glass vials (20 ml), each of which was capped with a septum and tightly sealed before being placed upside-down on a needle rack with a small additional needle for venting. The needle rack supplies a continuous flow of N_2 for at least 3 h to replace the internal atmosphere and dissolved gases with pure N_2. The bacteria vials were removed from the rack, and the oxidized sample (~0.5 ml) was injected into each bacteria vial. Once injected, the bacteria vials were kept in the dark for 2–3 h to ensure the quantitative transformation of nitrate (NO_3^-) to nitrous oxide (N_2O) before being frozen at −21 °C.

On the day of analysis, the bacteria were thawed, lysed with several drops of 10 N sodium hydroxide and placed on a mass spectrometer for isotope analysis. The $\delta^{15}N$ value of the N_2O was determined using a custom-built inlet system automated for extraction and purification coupled to a Thermo MAT253 Plus stable isotope ratio mass spectrometer[80,81]. Long-term precision was determined by analysing internal coral standards with each sample batch, which yielded an average carbonate standard reproducibility of ±0.2‰.

Coral oxygen isotopes

Oxygen isotopes were measured on coral cores from Martinique, Belize and Costa Rica (Supplementary Fig. 2). For each run, 55 coral carbonate samples of 100–200 µg were analysed for $\delta^{18}O$ in the inorganic stable isotope laboratory at the MPIC in Mainz. One International Atomic Energy Agency carbonate standard (IAEA-603) ($n = 10$) and one Virje University Internal Carbonate Standard (VICS) ($n = 11$) were used to calibrate the analyses to the Vienna PeeDee Belemnite (VPDB) scale. Samples were measured using an isotope ratio mass spectrometer (Delta V Advantage, Thermo Scientific) which is connected to a GasBench II unit (Thermo Scientific). Each sample was placed in a 12 ml Exetainer vial (part no. 9RK8W; Labco). Samples and standards were then put into a hot block heated to 70 °C. First, the vials are flushed with helium to remove atmospheric CO_2. Then, >99% H_3PO_4 (5–10 drops) was added and the sample was left to dissolve for 1.5 h. Finally, the sample was transferred in helium carrier gas to the GasBench II unit, where water and contaminant gases were removed before subsequent isotope analysis using the isotope ratio mass spectrometer. The average analytical precision, based on the reproducibility of IAEA-603, was 0.11‰ (1s.d., $n = 42$) for oxygen isotopes and 0.09‰ (1s.d., $n = 42$) for carbon isotopes.

Age model

The $\delta^{18}O$ data for samples from Martinique, Belize and Costa Rica were calibrated against their respective OIv2SST dataset (taken from https://climexp.knmi.nl/start.cgi). The highest $\delta^{18}O$ values were anchored to the lowest SST, which translates to February at Caye d'Olbian, Martinique and at Turneffe Atoll, Belize, and January at Cahuita, Costa Rica, whereas the lowest $\delta^{18}O$ values were anchored to the highest SST, which served as the basis of our age model. The $\delta^{18}O$ and SST yield a negative correlation with SST of −0.15‰ per °C ($r^2 = 0.65$) for Martinique, −0.18‰ per °C ($r^2 = 0.56$) for Belize and −0.28‰ per °C ($r^2 = 0.46$) for Costa Rica (Supplementary Fig. 3). Age models for annually resolved records had already been established for samples from Bermuda[47], Cuba[82] and Tobago[83], whereas X-ray density bands were used for the coral core from Mexico.

Analysis of seawater nutrient concentrations

Water samples were collected between December 2022 and March 2023 using a rosette water sampler equipped with five five-litre bottles according to the protocol detailed in Schiebel et al.[84]. The sampling was conducted along an east–west transect across the Atlantic at 13° N and across the Caribbean Sea at 11° N during a cruise aboard the research sailing yacht *Eugen Seibold* (https://www.mpic.de/4224334/sy-eugen-seibold). All water samples were frozen on collection and kept frozen at −21 °C until analysis.

Analyses for NO_3^-, nitrite (NO_2^-) and phosphate (PO_4^{3-}) were conducted at the MPIC. Concentrations of NO_3^- and NO_2^- were first determined according to Braman and Hendrix[85] using a nitrogen oxides analyser (T200, Teledyne API) with a detection limit of 0.01 µM and a precision (±1s.d., $n = 55$) of 0.55%. The PO_4^{3-} concentrations were determined using a continuous flow autoanalyser (QuAAtro, Seal Analytical) with a detection limit of 0.01 µM and a precision (±1s.d., $n = 55$) of 0.5%. For the GO-SHIP A20 (EXPOCODE: 325020210316) and A22 (EXPOCODE: 325020210420) samples, the concentration data were generated as part of the GO-SHIP programme and accessed via the CCHDO Hydrographic Data Office (US San Diego Library Digital Collections; CCHDO Hydrographic Data Archive, 2023, https://doi.org/10.6075/J0CCHAM8).

Analysis of seawater nitrogen isotopes

The $\delta^{15}N$ values of $NO_3^- + NO_2^-$ and NO_3^--only were measured using the denitrifier method[77,80] in the Martínez-García Laboratory (MPIC; for the *Seibold* samples) and at Princeton University (for the GO-SHIP A20

and A22 samples), following the protocols of ref. 81. NO_3^- + NO_2^- or NO_3^- (2–20 nmol N depending on concentration) was quantitatively converted to N_2O gas by a strain of denitrifying bacteria (*Pseudomonas aureofaciens*) that lacks active N_2O reductase enzymes. The $\delta^{15}N$ of N_2O was determined using the previously described purpose-built inlet system coupled to the Thermo MAT253 Plus stable isotope ratio mass spectrometer[77,80,81].

Excess phosphorus data

Excess P, expressed as $P^* = PO_4^{3-} - NO_3^-/16$ (ref. 19), was calculated from nutrient measurements compiled in the GLODAPv2.2022 (Global Ocean Data Analysis Project version 2.2022) dataset between 1983 and 2020. These data were based on cruises that have reliably measured NO_3^- and PO_4^{3-} in the North Atlantic (−10 to 30° N, 20 to 60° W). To avoid seasonal biases, only years with sufficient data throughout the year and covering the whole latitudinal range were included (Supplementary Fig. 4). Values were depth-integrated until reaching the pycnocline. The pycnocline depth was calculated based on the POAMA/PEODAS analysis z20 dataset taken from the Climate Explorer website (https://climexp.knmi.nl).

Sargassum biomass estimation

The methods for estimating *Sargassum* biomass from satellite observations since 2000 have been detailed in Wang et al.[86] and Hu and et al.[87]. Briefly, satellite images were analysed to examine the image features (that is, spatial anomalies), and these image features were delineated using a computer deep-learning model (Hu et al.[87]). The spectral shapes of these delineated image features, relative to the surrounding seawater, were examined to determine the presence of *Sargassum*. The amount of *Sargassum* within each image pixel was first estimated as a percentage cover, and then converted to wet biomass using a field-determined calibration constant[86]. Finally, many satellite images within a month were used to remove data gaps (due to clouds and other factors) and to calculate the average biomass at a given location.

Dust and black carbon model

The EMAC (ECHAM5/MESSy2 Atmospheric Chemistry)[88] was used to calculate wet and dry depositions of mineral dust and black carbon over the equatorial North Atlantic (0 to 20° N, 20 to 60° W) for the period 2003–2019. The EMAC model describes tropospheric and middle atmosphere processes, and their interactions with the land and oceans. For this work, we used the DDEP (Dry DEPosition) submodel[89] to estimate dry deposition, whereas the SCAV (SCAVenging) submodel was used to simulate wet deposition[90]. A detailed description and evaluation regarding the EMAC configuration and the submodels used in this study can be found in Holanda et al.[91], in which the black carbon calculations are also evaluated against observations. A detailed evaluation of the model performances in reproducing dust transport can be found in Abdelkader et al.[92].

Caribbean CB-$\delta^{15}N$ stack

A master CB-$\delta^{15}N$ record was constructed using the records within the mean Caribbean nitrate $\delta^{15}N$ (Extended Data Fig. 3), which includes Cuba, Martinique, Belize and Mexico. This ensured that the variability within each record was probably driven by natural processes and reduced the inclusion of local anthropogenic effects, for example, terrestrial runoff. Nevertheless, it is worth indicating that the record from Mexico showed a disagreement with the other selected records around the 1980s; this coincides with a period of very sudden and rapid development in the area that may have temporarily affected the record. The master record was constructed from normalized CB-$\delta^{15}N$ time series (normalized CB-$\delta^{15}N$ = [(CB-$\delta^{15}N$ − average CB-$\delta^{15}N$)/(standard deviation of CB-$\delta^{15}N$)]) and then smoothed with a Gaussian filter using the SciPy package (v.1.11.2).

Cuba—the dataset with the longest continuous record (1900–2015)—was selected as the base time series, to which the other three records were sequentially integrated. Where overlaps occurred, data points were averaged to mitigate any abrupt transitions. This averaging was weighted by the confidence levels of the original data that were provided by each source. For example, data points with a confidence level of 95% will contribute more to the average than those with a confidence level of 75%. When calculating the overall confidence level, error propagation was applied by considering the individual CB-$\delta^{15}N$ record confidence levels and then taking the square root of the sum of the squared individual errors. The final composite (master CB-$\delta^{15}N$) time series was analysed to identify significant temporal trends and anomalies.

Statistical analysis

CB-$\delta^{15}N$ values were imported to a Python3 Jupyter Notebook (v.5.7.4) using the Pandas software library. Data were plotted with Seaborn/Matplotlib and reprocessed for wavelet analysis according to the waipy script (https://github.com/mabelcalim/waipy). The continuous wavelet transform significance test was based on Torrence and Compo[93], and cross wavelet analysis was based on Maraun and Kurths[94]. LOESS of isopycnic P* values was conducted in the Python3 Jupyter Notebook (v.5.7.4) with >1,000 bootstraps to provide a better characterization of the uncertainty in the estimates. Linear and multiple regressions and AIC analyses to understand the relationship between abiotic environmental conditions and *Sargassum* blooms were all conducted using RStudio (v.4.3.0). Correlations are expressed as adjusted *r*-squares. Unlike *r*-squared, adjusted *r*-squared increases only if the new predictor enhances the model more than would be expected by chance. It can also decrease if a predictor improves the model by less than expected by chance. Standard deviations are given as ±1s.d.

Ethics and inclusion statement

This study was conducted ensuring fairness, respect, care and honesty throughout the research process. Local collaborators were engaged as equal partners in the design, execution and interpretation of the study, with co-authorship offered in recognition of substantive contributions. Fieldwork was carried out with the appropriate research permits and in close collaboration with local institutions and stakeholders. Training and mentorship opportunities were provided to early-career scientists and students, with particular emphasis on capacity building in the regions where data were collected. All data and findings will be shared transparently with local partners and relevant authorities to support both scientific knowledge and local conservation efforts. We are committed to equitable knowledge exchange, avoiding exploitation of local resources or communities and ensuring that the benefits of this research extend to the regions in which it was conducted.

Data availability

All data are publicly available via Dryad at https://doi.org/10.5061/dryad.jm63xsjkq (ref. 95).

Code availability

Codes used for the figures and data analyses are available via GitHub at https://github.com/marinejon/Equatorial-upwelling-of-phosphorus-drives-Atlantic-N2-fixation-and-Sargassum-blooms and via Dryad at https://doi.org/10.5061/dryad.jm63xsjkq (ref. 95).

References

77. Sigman, D. M. et al. A bacterial method for the nitrogen isotopic analysis of nitrate in seawater and freshwater. *Anal. Chem.* **73**, 4145–4153 (2001).
78. Wang, X. T. et al. Isotopic composition of carbonate-bound organic nitrogen in deep-sea scleractinian corals: a new window into past biogeochemical change. *Earth Planet. Sci. Lett.* **400**, 243–250 (2014).

79. Moretti, S. et al. Analytical improvements and assessment of long-term performance of the oxidation–denitrifier method. *Rapid Commun. Mass Spectrom* **38**, e9650 (2024).
80. Casciotti, K. L., Sigman, D. M., Galanter Hastings, M., Böhlke, J. K. & Hilkert, A. Measurement of the oxygen isotopic composition of nitrate in seawater and freshwater using the denitrifier method. *Anal. Chem.* **74**, 4905–4912 (2002).
81. Weigand, M. A., Foriel, J., Barnett, B., Oleynik, S. & Sigman, D. M. Updates to instrumentation and protocols for isotopic analysis of nitrate by the denitrifier method. *Rapid Commun. Mass Spectrom* **30**, 1365–1383 (2016).
82. Alonso-Hernández, C. M. et al. Registro de temperatura superficial del mar (1778–2015) en *Orbicella faveolata* (Cnidaria: Scleractinia) del arrecife Cayo Santa María, Cuba. *Rev. Invest. Mar.* **42**, 37–53 (2022).
83. Ong, M. R., Goodkin, N. F., Guppy, R. & Hughen, K. A. *Colpophyllia natans* from Tobago, a novel paleoclimate archive for reconstructing sea surface temperature in the tropical Atlantic. *Paleoceanogr. Paleoclimatol.* **37**, e2022PA004483 (2022).
84. Schiebel, R. et al. Preface: special issue on probing the open ocean with the research sailing yacht *Eugen Seibold* for climate geochemistry. *J. Geophys. Res. Atmos.* **129**, e2023JD040581 (2024).
85. Braman, R. S. & Hendrix, S. A. Nanogram nitrite and nitrate determination in environmental and biological materials by vanadium (III) reduction with chemiluminescence detection. *Anal. Chem.* **61**, 2715–2718 (1989).
86. Wang, M. et al. Remote sensing of *Sargassum* biomass, nutrients, and pigments. *Geophys. Res. Lett.* **45**, 12,359–12,367 (2018).
87. Hu, C. et al. Mapping and quantifying pelagic *Sargassum* in the Atlantic Ocean using multi-band medium-resolution satellite data and deep learning. *Remote Sens. Environ.* **289**, 113515 (2023).
88. Jöckel, P. et al. Development cycle 2 of the Modular Earth Submodel System (MESSy2). *Geosci. Model Dev.* **3**, 717–752 (2010).
89. Kerkweg, A. et al. Technical note: an implementation of the dry removal processes DRY DEPosition and SEDImentation in the Modular Earth Submodel System (MESSy). *Atmos. Chem. Phys.* **6**, 4617–4632 (2006).
90. Tost, H., Jöckel, P., Kerkweg, A., Sander, R. & Lelieveld, J. Technical note: a new comprehensive SCAVenging submodel for global atmospheric chemistry modelling. *Atmos. Chem. Phys.* **6**, 565–574 (2006).
91. Holanda, B. A. et al. African biomass burning affects aerosol cycling over the Amazon. *Commun. Earth Environ.* **4**, 154 (2023).
92. Abdelkader, M. et al. Sensitivity of transatlantic dust transport to chemical aging and related atmospheric processes. *Atmos. Chem. Phys.* **17**, 3799–3821 (2017).
93. Torrence, C. & Compo, G. P. A practical guide to wavelet analysis. *Bull. Am. Meteor. Soc.* **79**, 61–78 (1998).
94. Maraun, D. & Kurths, J. Cross wavelet analysis: significance testing and pitfalls. *Nonlinear Process. Geophys.* **11**, 505–514 (2004).
95. Jung, J. et al. Equatorial upwelling of phosphorus drives Atlantic N_2 fixation and *Sargassum* blooms. *Dryad* https://doi.org/10.5061/dryad.jm63xsjkq (2025).

Acknowledgements

We thank B. Hinnenberg, M. Schmitt and F. Rubach for technical support during sample preparation and analyses. We thank G. Heiss and M. Hassan for their invaluable assistance during the fieldwork, and R. Leinfelder for helping to secure the funding necessary for collecting the Martinique record. We thank M. Berger, M. K. Donovan, A. Frazier, K. Cramer and A. O'Dea for helping to secure permits for the Panama and Belize species intercalibration. We extend our thanks to the crew of the sailing yacht *Eugen Seibold*, all of whom have substantially contributed to the success of the sampling campaign. We thank the chief scientists of the GO-SHIP A20 and A22 cruises in 2021, R. Woosley and V. Menezes, as well as their crews, and acknowledge the support of the US-GOSHIP programme. Data were collected and made publicly available by the US Global Ship-based Hydrographic Investigations Program (US GO-SHIP; https://usgoship.ucsd.edu/) and the programmes that contribute to it. We are grateful to S. E. Fawcett and V. H. Luu for the nitrogen isotope measurements of *Sargassum* from the subtropical North Atlantic in Extended Data Fig. 1. This project was funded by the Max Planck Society (J.J., N.N.D., A.D.F., H.V., R.S., G.H.H.); the German Research Foundation (DFG) project no. 468591845 (A.M.-G.); SPP 2299/project no. 441832482; the Paul Crutzen Nobel Prize Fellowship (N.N.D.); the "Bourse régionale de la découverte" de la Région Poitou-Charentes, France (N.N.D.); the Vice-Rectory of Research, University of Costa Rica, project no. 808-A8-602 (C.J.); the German Research Foundation (DFG) project no. Gi 222/5-1 (E.G.); European Horizon 2020 MaCoBioS (grant 869710; J.P.D., G.O.C.); the US National Science Foundation grant 1903586 (N.F.G.); the Niarchos Foundation (N.F.G., R.G.); NASA grant 80NSSC25K7361 (B.B.B.); NASA grant 80NSSC24K1507 (C.H.); Schmidt Sciences, LLC (D.M.S.); FNRS-FRS EQP U.N029.23 ENGAGE (F.F.); FNRS CDR J.0083.25 ONIC (F.F.); and the FWB ARC Consolidation Project STEREO (F.F.).

Author contributions

J.J. and A.M.-G. conceived the study and managed the project, with A.M.-G. providing supervision. The methodology was developed by J.J., A.M.-G., N.N.D., A.D.F., A.P., C. Pöhlker, B.R. and E.L.M. Investigation and visualization was led by J.J., with contributions from C. Pellio, F.F., Y.R., T.W., C.H., B.B.B. and A.M.-G. Funding was secured by G.H.H., R.S., C.H., B.B.B. and A.M.-G. Resources were provided by J.J., J.P.D., C. Pellio, G.O.C., B.R., D.K.K., E.L.M., C.J., E.G., P.M., C.A.-H., M.G.-B., C.T.-C., J.C., M.R.O., N.F.G., R.G., H.A., H.S., L.H., I.H.d.A., A.L.B., M.Y., T.P.N., K.J., D.S., J.R., C.H., B.B.B., A.P., C. Pöhlker, J.L., U.P., H.V. and R.S. The work was validated by J.J. and A.M.-G. The original paper was drafted by J.J., D.M.S. and A.M.-G., and all authors contributed to the review and editing.

Funding

Open access funding provided by Max Planck Society.

Competing interests

The authors declare no competing interests.

Additional information

Extended data is available for this paper at https://doi.org/10.1038/s41561-025-01812-2.

Supplementary information The online version contains supplementary material available at https://doi.org/10.1038/s41561-025-01812-2.

Correspondence and requests for materials should be addressed to Jonathan Jung or Alfredo Martínez-García.

Peer review information *Nature Geoscience* thanks David Baker, Thierry Moutin and the other, anonymous, reviewer(s) for their contribution to the peer review of this work. Primary Handling Editor: James Super, in collaboration with the *Nature Geoscience* team.

https://doi.org/10.1038/s41561-025-01812-2

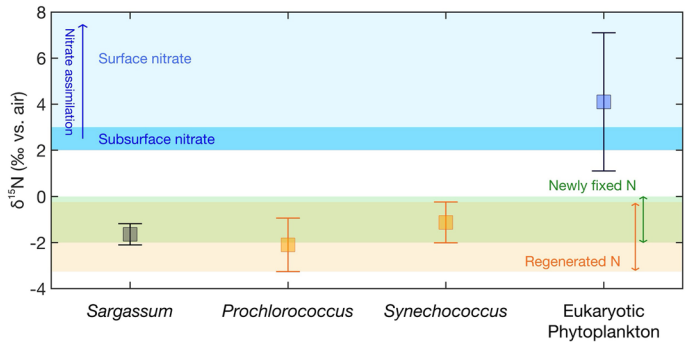

Extended Data Fig. 1 | Nitrogen isotope values of *Sargassum*, *Prochlorococcus*, *Synechococcus*, and Eukaryotic Phytoplankton from the subtropical North Atlantic. The nitrogen isotope values of the macroalgae *Sargassum* fall with values for the ubiquitous marine cyanobacteria *Prochlorococcus* and *Synechococcus*. Common eukaryotic phytoplankton fall above that seen of *Sargassum* based on data by ref. 31. The ranges of regenerated N, newly fixed N, subsurface nitrate and surface nitrate are indicated by colored bars. The lower and upper bound of the error bar represent the full range of data.

https://doi.org/10.1038/s41561-025-01812-2

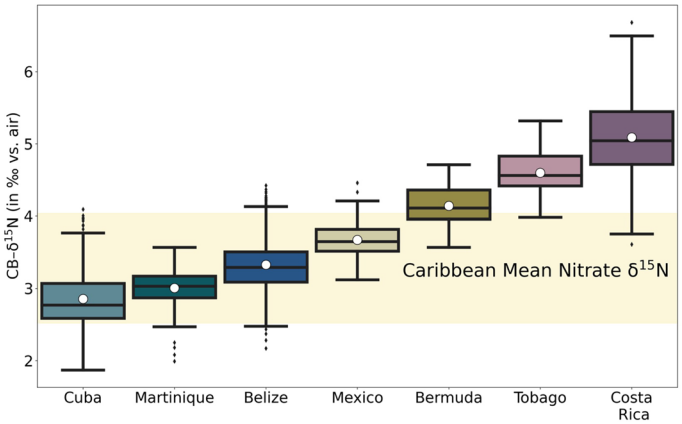

Extended Data Fig. 2 | Coral-bound $\delta^{15}N$ distribution across the Wider Caribbean. Boxplots based on 2507 newly measured CB-$\delta^{15}N$ values (in ‰ vs. air) grouped according to the coral core location and compared to the mean Caribbean nitrate $\delta^{15}N$ (3.28 ± 0.76‰) as indicated by the horizontal shaded area. CB-$\delta^{15}N$ values for Bermuda are based on Wang et al. (2015). Values above mean Caribbean nitrate $\delta^{15}N$ indicate regions that are suspected to be influenced by local conditions. The white dot represents the average value whereas the middle line represents the median value. The lower and upper bound of the box correspond to the first and third quartiles. The upper whisker extends from the upper bound box to the largest value within 1.5 times the inter-quartile range (IQR) from the hinge, while the lower whisker extends from the lower bound box to the smallest value within 1.5 times the IQR from the hinge. Values beyond the whiskers are considered outliers and are plotted individually.

https://doi.org/10.1038/s41561-025-01812-2

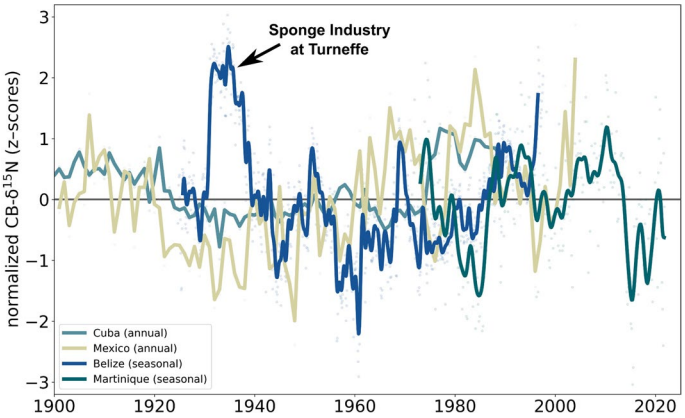

Extended Data Fig. 3 | Normalized (z-scores) CB-δ^{15}N timeseries. The compilation is based on the measured coral cores that were used for the stacked record. Raw CB-δ^{15}N values were standard score normalized (z-score) according to the normalized CB-δ^{15}N = [(CB-δ^{15}N - average CB-δ^{15}N) / (standard deviation of CB-δ^{15}N)]. A Gaussian smoothing was applied to each CB-δ^{15}N timeseries to highlight the low-frequency shared natural variability between each location.

https://doi.org/10.1038/s41561-025-01812-2

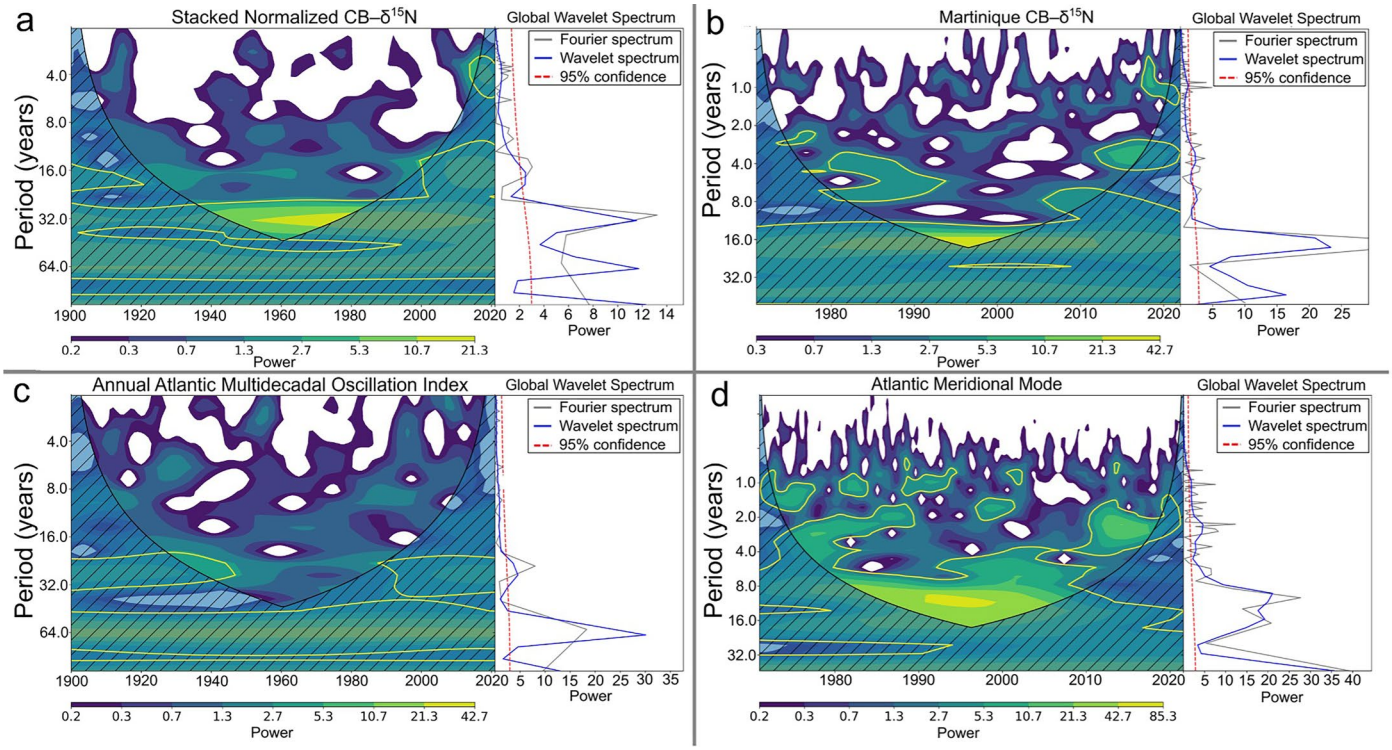

Extended Data Fig. 4 | Continuous Wavelet Transformation plot of the master CB-δ^{15}N record and the AMO as well Martinique CB-δ^{15}N record and the AMM. **a**, Continuous Wavelet Transformation plot and Cross Wavelet Analysis of the normalized master CB-δ^{15}N and **b**, the CB-δ^{15}N record from Martinique versus **c**, the low frequency Atlantic Multidecadal Oscillation (AMO) index and **d**, the high frequency Atlantic Meridional Mode (AMM) index. The period corresponds to years and yellow contours significant periods.

https://doi.org/10.1038/s41561-025-01812-2

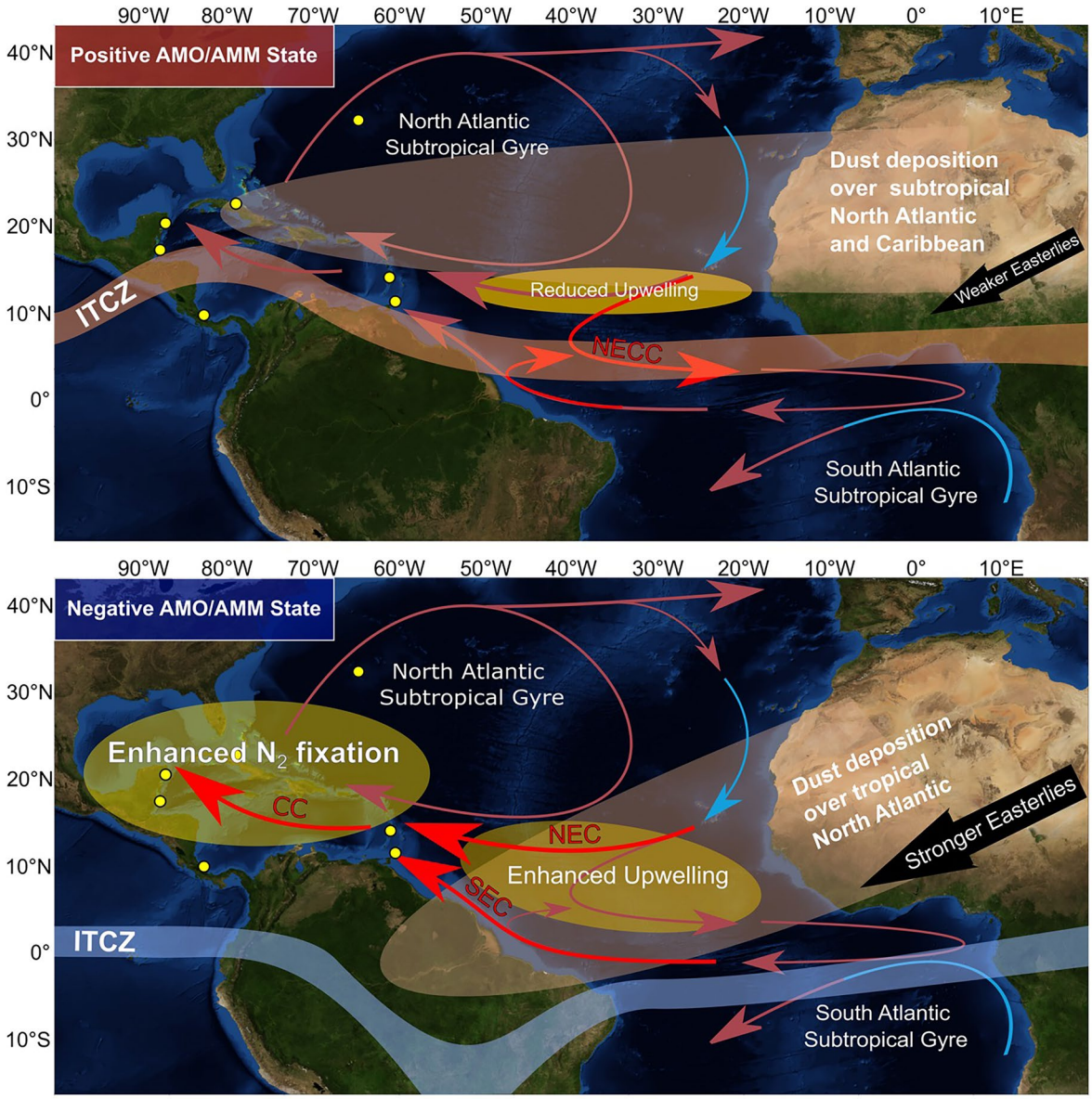

Extended Data Fig. 5 | Schematic of ocean-atmosphere dynamics during positive and negative AMO/AMM states. Schematic overview of the ITCZ position, the Saharan dust plume, and surface currents during positive (top) and negative (bottom) AMO/Atlantic Meridional Mode (AMM) phases. Positive AMO/AMM phases correspond to a northward displacement of the ITCZ, a predominance of the Saharan dust plume over the subtropical North Atlantic and Caribbean, reduced easterly wind strength, and an enhanced North Equatorial Counter Current (NECC). Negative AMO/AMM phases correspond to a southward displacement of the ITCZ, a predominance of Saharan dust over the equatorial North Atlantic and Amazon basin, and stronger easterlies that enhance equatorial upwelling. Also, during negative AMO/AMM phases the North Equatorial Current (NEC), the South Equatorial Current (SEC) and the Caribbean Current (CC) are stronger and transport more Atlantic water with excess P into the Caribbean, ultimately enhancing N2 fixation. Base map: 'Blue Marble' global mosaic. Credit: NASA's Goddard Space Flight Center.

https://doi.org/10.1038/s41561-025-01812-2

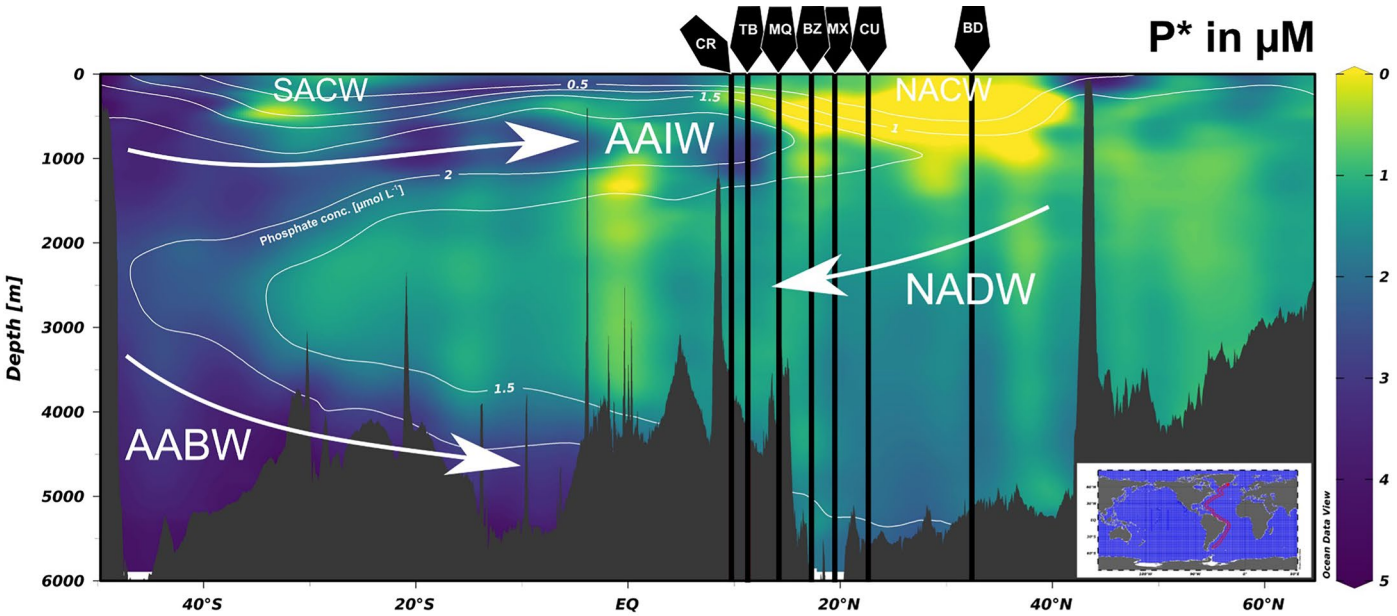

Extended Data Fig. 6 | North–south depth profile of excess P in the Atlantic. Excess P (expressed as P* = PO_4^{3-}-NO_3^-/16 in µM) against water depth in a north–to–south transect along the western margin of the Atlantic Ocean (adapted after Deutsch et al. 2007). Positive P* values indicate excess P and are plotted in relation to P concentrations (in µmol L^{-1}, shown as iso–concentration lines). Coral core locations are shown on top with respect to their latitude (CR = Costa Rica; TB = Little Tobago; BZ = Belize; CU = Cuba; BD = Bermuda; MQ; Martinique; MX = Puerto Morelos. SACW – South Atlantic Central Water, NACW – North Atlantic Central Water, AAIW – Antarctic Intermediate Water, NADW – North Atlantic Deep Water, AABW – Antarctic Bottom Water. Basemap created with Ocean Data View v.5.6.3 (https://odv.awi.de).

https://doi.org/10.1038/s41561-025-01812-2

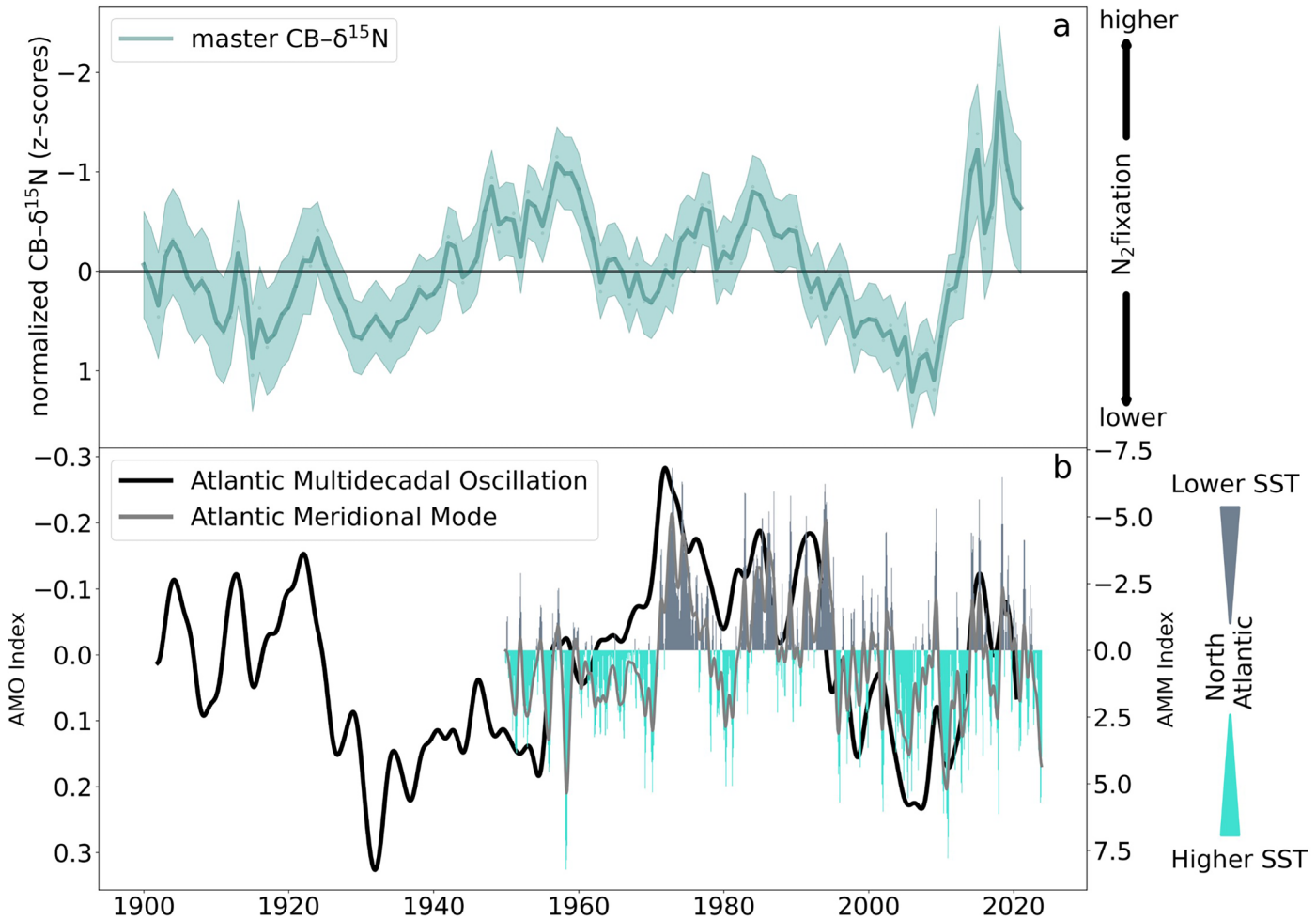

Extended Data Fig. 7 | Coral-bound $\delta^{15}N$ master record versus AMO and AMM index. a, The stacked normalized CB-$\delta^{15}N$ record in relation to the **b**, Atlantic Meridional Mode index based on Chiang and Vimont, 2004[3]. The Atlantic Multidecadal Oscillation is superimposed to show interrelations. Positive AMM states are indicated in grey and correspond to higher north-equatorial SST and easterly wind stress whereas negative AMM states are indicated in light blue and correspond to lower north–equatorial SST and higher easterly wind stress.

https://doi.org/10.1038/s41561-025-01812-2

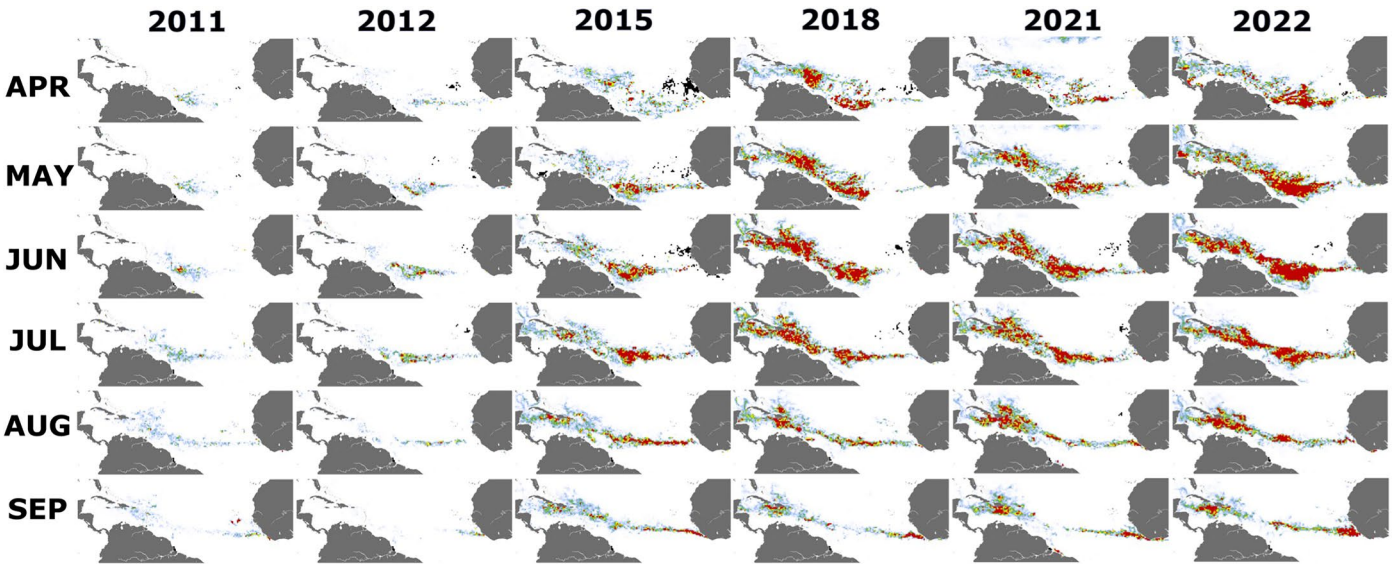

Extended Data Fig. 8 | Monthly *Sargassum* spp. extents for the years 2011, 2012, 2015, 2018, 2021, and 2022. Based on remote sensing data, the main growth season starts during April concomitant with the yearly minimum AMM state. Extensive growth bands are evident starting in April and lasting until late September, with a tendency to increasing *Sargassum* extents trends over time.

https://doi.org/10.1038/s41561-025-01812-2

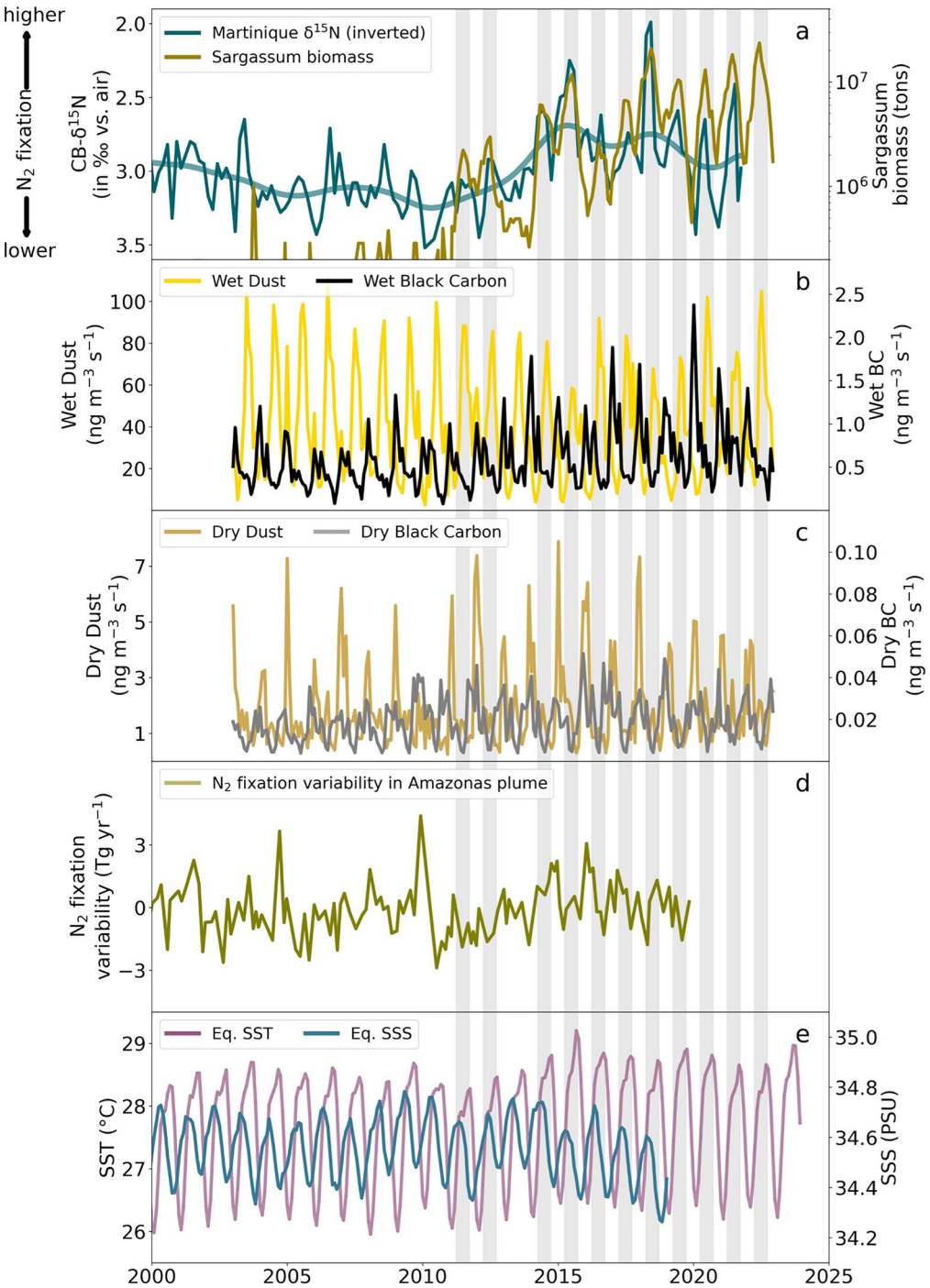

Extended Data Fig. 9 | Martinique CB-δ^{15}N record and alternative environmental parameters used to explain Sargassum blooms. a, CB-δ15N values (in ‰ vs. air) of the coral core taken from Martinique in relation to the logarithmic Sargassum spp. biomass of the equatorial Atlantic and Caribbean (0–20°N, 40–90°W). **b**, Area weighed (10–20°N, 20–60°W) dry dust and dry black carbon deposition (ng m-3 s-1), calculated with the EMAC model. **c**, Area weighed (10–20°N, 20–60°W) wet dust and wet black carbon deposition (ng m-3 s-1), also based on the EMAC model. **d**, Average modelled N2 fixation variability (in Tg N yr-1) in the Amazonas plume as taken from Härri et al. 2024. **e**, Equatorial North Atlantic (0 to 20°N, 20°W to 60°W) SST (°C) is based on the OIv2SST dataset and SSS (PSU) is taken from https://climexp.knmi.nl/.

https://doi.org/10.1038/s41561-025-01812-2

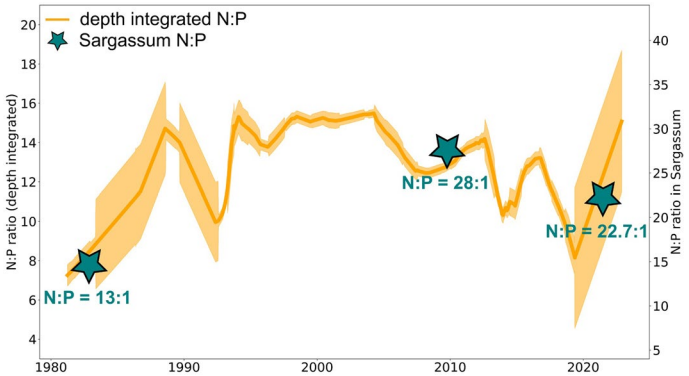

Extended Data Fig. 10 | Depth integrated (to pycnocline) N:P ratios in Sargassum biomass and in waters of the equatorial North Atlantic. Previous studies attributing changes in N:P ratios in Sargassum biomass to anthropogenic N-enrichment by Lapointe et al., 2021 appear to follow mostly natural nutrient availability in waters of the equatorial North Atlantic when including Sargassum biomass N:P data from McGillicuddy et al., 2023. Note that N:P in Sargassum is twice as high as the water.